Article

Crystallographic Study of Transformation Products of Heat-Affected Zone and Correlation with Properties of FH690 Heavy-Gauge Marine Steel by Multi-Pass Submerged Arc Welding

Yun Bai [1,2], Liqin Bai [3], Gang Qian [2], Xianjin Sun [2,*], Guanyou Liu [2], Zhenjia Xie [4,*] and Chengjia Shang [4]

1   School of Metallurgical and Ecological Engineering, University of Science and Technology Beijing, Beijing 100083, China
2   Research Institute of Jiangyin Xingcheng Special Steel Works Co., Ltd., Jiangyin 214429, China
3   Collaborative Innovation Center of Steel Technology, University of Science and Technology Beijing, Beijing 100083, China
4   State Key Laboratory for Advanced Metals and Materials, University of Science and Technology Beijing, Beijing 100083, China
*   Correspondence: sunxianjin@citicsteel.com (X.S.); zjxie@ustb.edu.cn (Z.X.)

Abstract: In this work, the microstructure–property relationship of the heat-affected zone (HAZ) of a FH690 ultra-heavy marine steel plate was investigated based on insight of microstructure and crystallographic features. After multi-pass welding with a heat input of ~30 kJ/cm, an ~8 mm wide HAZ was obtained with a coarse grain HAZ (CGHAZ) of ~3.8 mm, fine grain HAZ (FGHAZ) of ~3.4 mm, and intercritical HAZ (ICHAZ) of ~1 mm. High impact toughness values of ~120 and 140 J at −60 °C were obtained for coarse grain HAZ and fine grain HAZ, respectively. The microstructure of the CGHAZ and FGHAZ was fine lath bainite. Although the average prior austenite grain size for the CGHAZ was ~75 μm, which was five times that of the FGHAZ (15 μm), a high density of high-angle grain boundaries (HAGBs) with misorientation higher than 45° was obtained in the CGHAZ. This is the underlying reason for the excellent low-temperature toughness of the HAZ. Thermo-dynamic calculations indicated that the high density of HAGBs in the CGHAZ was attributed to the decreased bainitic transformation temperature due to the reduced phase transformation driving force via the high nickel addition, leading to weak variant selection. In addition, the high nickel addition offered high hardenability for high hardness in the FGHAZ. The outcome of this study could provide an experimental and fundamental basis for designing high-strength ultra-heavy steel plates with excellent weldability.

Keywords: crystallographic feature; FH690; HAZ; microstructure–property relationship; welding

1. Introduction

With the increasing requirement for large-scale and weight-saving marine engineering structures, there is a continuous increasing demand for ultra-heavy gauge steel plates with high yield strength and excellent low-temperature toughness [1–3]. In general, most high-strength–toughness ultra-heavy steel plates are produced by quenching and tempering, in which quenching produces lath bainite to provide high strength and tempering modifies the low-temperature toughness [4,5]. However, welding is necessary during building marine engineering structures. And heat treatment is not easy to be carried out for large-scale structures. Therefore, the high strength–toughness of a welded joint of an ultra-heavy steel plate is of great importance for safety.

Although new methods, such as laser welding have been developed for thin alloys [6,7], multi-pass submerged arc welding is still the main method applied for welding ultra-heavy low-alloy steels. For welded joints of ultra-heavy steel plates, the mechanical properties concerning high strength and good toughness can be tailored using the thermal

cycles experienced during multi-pass welding, unavoidably producing local brittle zones with deteriorated toughness and local soft areas with low hardness [8,9]. Among those local brittle zones and soft areas, the CGHAZ always exhibits the worst toughness, and the FGHAZ usually presents the lowest hardness. The reasons for the deteriorated toughness of the CGHAZ have been widely studied. This has revealed that incomplete bainitic transformation usually occurs at intermedium temperature for the CGHAZ, leading to the formation of large martensite/austenite (M/A) constituents, which deteriorate the low-temperature toughness dramatically [10]. And the reason for softening in the FGHAZ has been attributed to the low hardenability when grain is very fine [11]. Hence, improving the low-temperature toughness of the CGHAZ and hardness of the FGHAZ is of great importance for ensuring a high safety of welded joints.

To obtain a good toughness in the CGHAZ, micro-size second-phase particles, such as TiN, ZrO_2, MgO, and Al_2O_3, are introduced to steels [12]. On one hand, the micro-size second-phase particles can act as pinning particles to slow the grain growth, leading to the refinement of grain size in the CGHAZ. On the other hand, those second particles can act as intergranular nucleation sites for acicular ferrite, resulting in further refinement of the grain size. However, a high density of micro-size particles usually deteriorates the low-temperature toughness of high-strength steel plates. Moreover, acicular ferrite cannot ensure a high strength greater than 690 MPa. Recently, tailoring variant selection behavior for producing a high density of HAGBs has been investigated by modifying the alloying composition. In ultra-low carbon steels, it is suggested that a high carbon content (0.06%) offers a higher density of HAGBs and better toughness than that with low carbon content (0.03%) [13]. Moreover, it has been revealed that nickel addition promotes the formation of V1/V2 variant pairs, leading to a high density of HAGBs and good toughness [14]. In the present work, we developed a 120 mm ultra-heavy FH690 high-strength steel plate accompanied with a good weldability using a high-nickel alloying design. The purpose of this work was to study the microstructure–property relationship of the heat-affected zone (HAZ) of the new FH690 ultra-heavy marine steel plate, with particular emphasis on the microstructure and crystallographic features. The findings of this study are expected to provide guidelines for alloying designs ensuring good weldability of ultra-heavy gauge high-strength–toughness steel plates.

2. Materials and Experimental Procedure

The chemical composition of the studied steel plate in a weight percent (wt%) was 0.13C-0.26Si-1.0Mn-0.41Cr-2.48Ni-0.55Mo-0.047Nb-0.012Ti-0.0015B. Relative low carbon and manganese contents were designed to ensure a low carbon equivalent (Ceq) for weldability. In addition, the low carbon and manganese contents can also be good for centerline segregation to ensure a good strength and toughness combination in the center region of the plate [15,16]. A high nickel content was used to ensure a good hardenability for the ultra-heavy plate. The steel was industrially processed via vacuum melting and continuous casting into slabs of 350 mm thickness. The slabs were manufactured to 120 mm thick plates by the classical two-stage controlled rolling. Then, the plates were reheated to 880 °C for full reaustenitization and quenched to room temperature. Finally, the quenched plates were tempered at 640 °C for 180 min, followed by air cooling to room temperature. Based on a previous study on the heat input on mechanical properties by simulated welding, ~30 kJ/cm was the best parameter for toughness. Therefore, multi-pass submerged arc welding (SAW) with the heat input of ~30 kJ/cm was carried out for welding. A part of the welded joint for this study is presented in Figure 1a.

Charpy impact test samples were prepared near the surface of the welded joint. A schematic image for the positions of Charpy impact test samples is presented in Figure 1. A Charpy impact test was carried out at −60 °C with the notch going through the fusion line (FL), and the HAZ with distances from the FL of 2, 5, 7, and 10 mm. Three specimens were measured for each zone, and the average impact energy was used for toughness. In addition, the Vickers hardness was measured for the HAZ. The HAZ was cut from the

welded joint for microstructure characterization. After mechanical grounding and polishing, the HAZ was etched using 4% nital for optical microscopy (OM) and scanning electron microscopy (SEM). SEM observations were carried out using a TESCAN MIRA 3 (TESCAN, Brno, Czech Republic) field-emission scanning electron microscope (FE-SEM). The mechanically polished samples were electropolished using a solution containing 85 vol% alcohol, 10 vol% perchloric acid, and 5 vol% glycerol for electron backscatter diffraction (EBSD) examination. EBSD analysis was performed with TESCAN MIRA 3 LMH FE-SEM equipped with an Oxford Symmetry EBSD (Oxford Instruments, Oxford, UK) detector at a voltage of 20 kV and a step size of 0.1 μm. ARPGE (version 2.4) software was employed for the reconstruction and visualization of prior austenite grains [17]. A Python program was employed for the statistical analysis of the interface density [18].
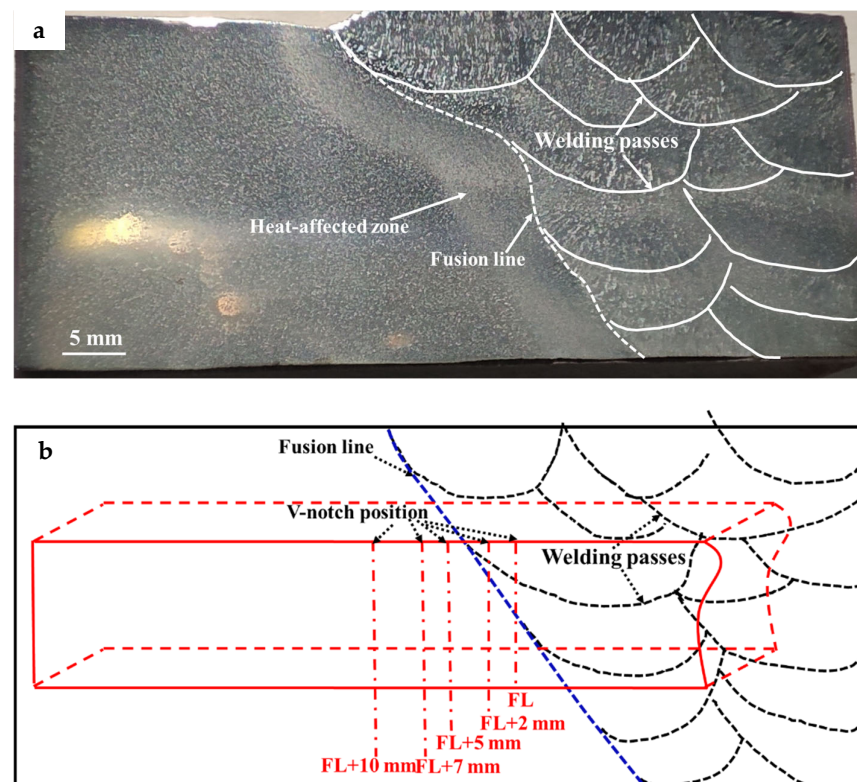

Figure 1. Real (**a**) and schematic (**b**) images showing the studied part of the multi-pass SAW welded joint.

3. Results and Discussion

3.1. Microstructure of the HAZ

After welding, the microstructure of the whole HAZ was examined by OM from weld metal to base metal. Figure 2 shows OM images for the HAZ of the studied welded joint. Figure 2a presents a whole view of the HAZ composed of several low magnification images. It can be seen that the HAZ can be divided into three zones according to their differences in contrast under optical observations at low magnification. From the weld metal to HAZ, lath bainite was observed in the CGHAZ, as shown in Figure 2b. Fine and dispersed carbides can be observed in the lath bainite matrix. This implies that the CGHAZ was tempered by the heat during later passes of welding. The faint prior austenite grain boundaries draw out the outline of grains with the largest diameter of ~125 μm. The width for the CGHAZ was ~3.8 mm. After the CGHAZ, a ~3.0 mm wide FGHAZ was obtained with a similar lath bainite microstructure, as shown in Figure 2a,c. The area connecting the FGHAZ and base metal was the intercritial HAZ, which was ~1 mm in width, as shown in Figure 2a. The microstructure in the intercritical HAZ consisted of a tempered bainite matrix and M/A

constituents, as shown in Figure 2d. The M/A constituents were dispersed along prior austenite grain boundaries.
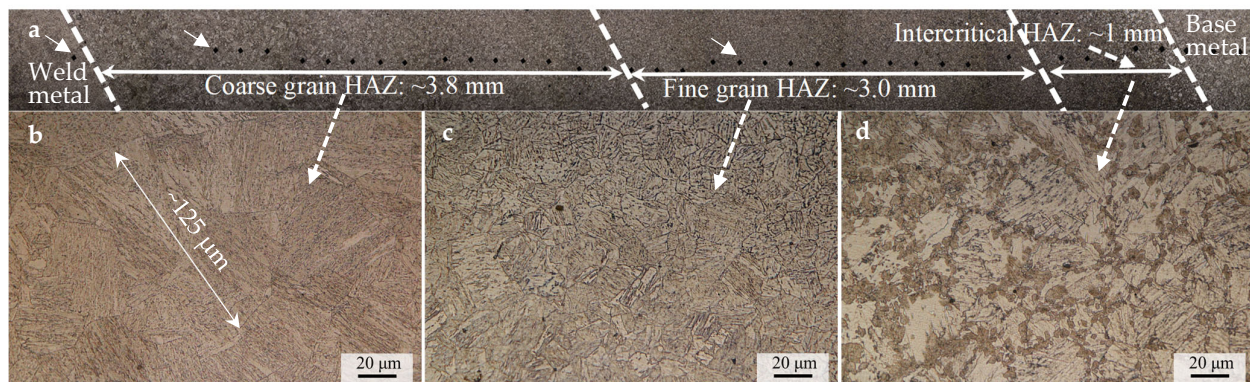

Figure 2. OM images showing the microstructure of the HAZ for the studied welded joint.

The microstructure of the studied welded joint was characterized by SEM for different heat-affected areas. The obtained results are presented in Figure 3. Figure 3a gives the SEM microstructure of the CGHAZ. It can be seen that lath bainite was obtained in the CGHAZ. The bainitic laths were straight and mostly ran through the whole grain. The bainitic laths had two morphology types. One was coarse bainite, and the other was fine bainite. It is suggested that the coarse bainite plates are formed by the coalescence of adjacent bainite sheaves with identical or similar orientation [19]. Among the fine bainitic lath matrix, very fine carbides in sphere shape were observed. The fine and sphere-shaped carbides may be good for both strength and toughness [20]. The FGHAZ and base metal presented a similar lath bainite microstructure for both coarse and fine bainite, as shown in Figure 3b,e, respectively. The bainitic lath boundaries in the base metal are blurred due to a long tempering time at the high temperature of 640 °C. Figure 3c,d show the SEM microstructure of the intercritical HAZ near to the FGHAZ and base metal, respectively. It can be found that the microstructure of the intercritical HAZ consisted of annealed bainite and newly formed lath bainite (which was characterized as M/A constituents in OM). The difference in microstructure for the areas near the FGHAZ and base metal was the volume fraction in the newly formed bainite/martensite. For the intercritical HAZ near the FGHAZ, the microstructure was reheated to the high temperature of the two-phase region during welding; thus, a large fraction of reverted austenite formed from the initial bainite, whereas the temperature experienced by the intercritical HAZ near the base metal was relatively low, such that the fraction of reverted austenite was small. During the subsequent cooling, those reverted austenite phases newly transformed to lath bainite. This is different from the publications in other low-carbon alloy steels with low nickel and high manganese additions [21]. In those steels, the reverted austenite usually transforms to hard martensite or M/A constituent due to the high enrichment of manganese. In the present work, the studied steel was alloyed with low manganese and high nickel. The low manganese contents made it difficult to obtain sufficient enrichment in reverted austenite to form martensite or M/A constituent. In addition, the diffusion coefficient of nickel is much slower than that of manganese, such that nickel was also difficult to diffuse into reverted austenite at the short duration period during welding [22,23]. Hence, the reverted austenite transformed to lath bainite in the same way as the base material. This may be helpful for obtaining a good low-temperature toughness in the intercritical HAZ.
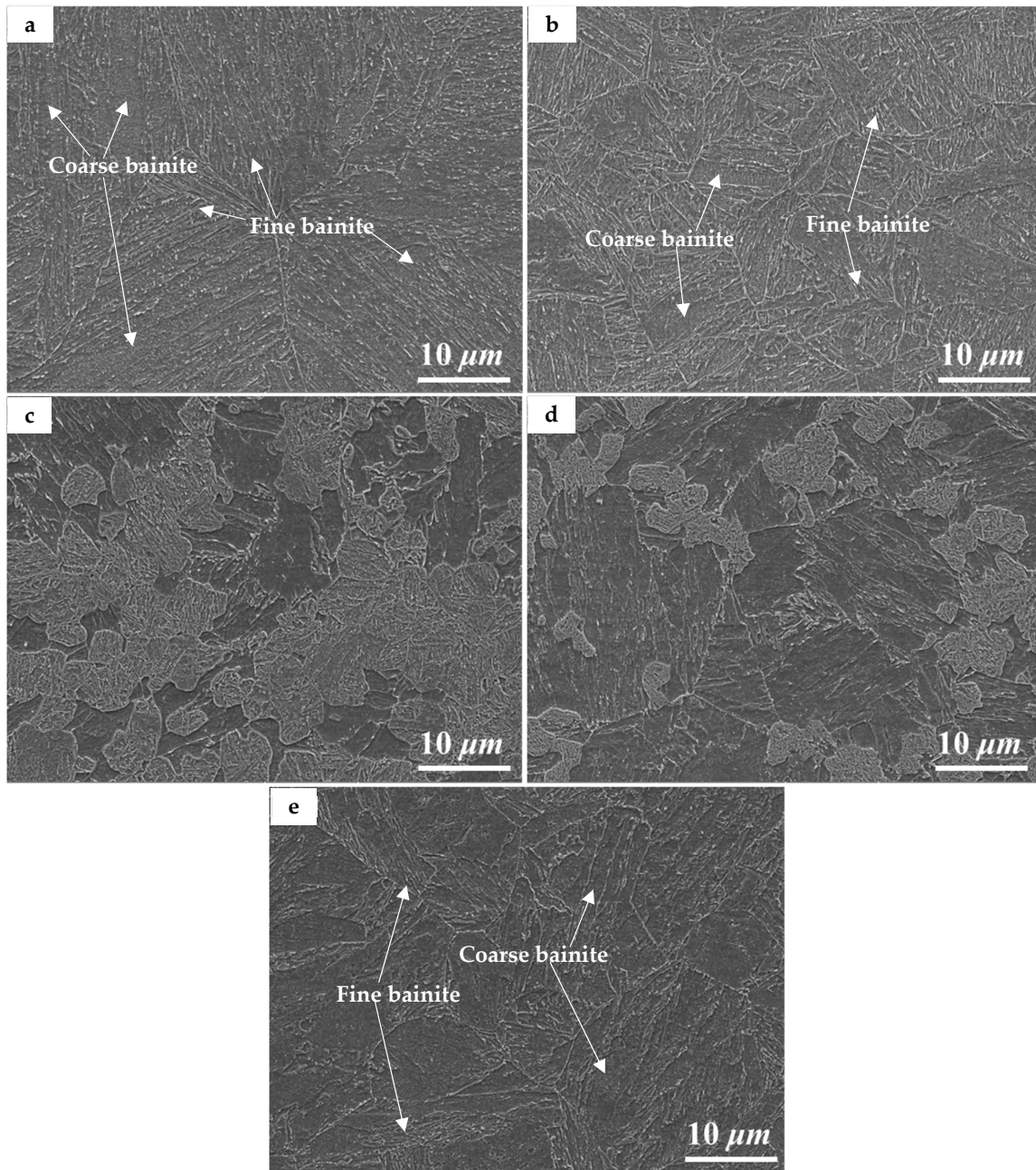
Figure 3. SEM images showing the microstructure of the HAZ for the studied welded joint: (**a**) CG-HAZ, (**b**) FGHAZ, (**c**,**d**) inctercritical HAZ, (**e**) base metal.

3.2. Mechanical Properties

Charpy v-notch impact toughness was measured for different zones of the studied welded joint at −60 °C. The obtained results of low-temperature impact energies of the FL, CGHAZ, FGHAZ, intercritical HAZ, and base metal are plotted in Figure 4. It can be clearly seen that the whole welded joint exhibited excellent low-temperature toughness. Although the impact toughness at the FL and inctercritical HAZ positions was slightly lower than that of the CGHAZ and FGHAZ, the average impact energies for all positions were higher than 100 J at −60 °C. The toughness of the FL is usually related to both the weld metal and CGHAZ. The related low-impact energy for the FL position may be caused by the weld metal. It is worth noting that the good Charpy impact toughness of ~103 ± 6 J for the intercritical HAZ was ascribed to the formation of a multiphase microstructure of annealed bainite and new lath bainite. This was totally different from our previous

studies on pipeline steels, in which large necklacing M/A constituents were formed in the intercritical HAZ, leading to the increased possibility of forming secondary microcracks and the change in fracture mode from ductile to quasi-cleavage fracture [24–26]. This implies that the low-manganese and high nickel addition was helpful for improving the low-temperature toughness of the intercritical HAZ. In addition, it is interesting that the CGHAZ had a similar good low-temperature toughness of ~125 ± 13 J to that of the FGHAZ (139 ± 9 J). Compared with single-pass welding, the effect of tempering induced by the lateral welding passes could have contributed to the high toughness obtained in this multi-pass welded joint, as observed in the tempered carbides in the fine lath bainite in the CGHAZ and FGHAZ (see Figure 3a,b). Moreover, it is suggested that the microstructure features, especially crystallographic features, play a determining role in controlling the fracture mode of the CGHAZ during low-temperature impact testing [27]. A high density of HAGBs offers a ductile fracture and high impact toughness. Therefore, the crystallographic features of the CGHAZ and FGHAZ were comparatively studied later in this work, and the mechanism of the formation of crystallographic features will be discussed in detail.
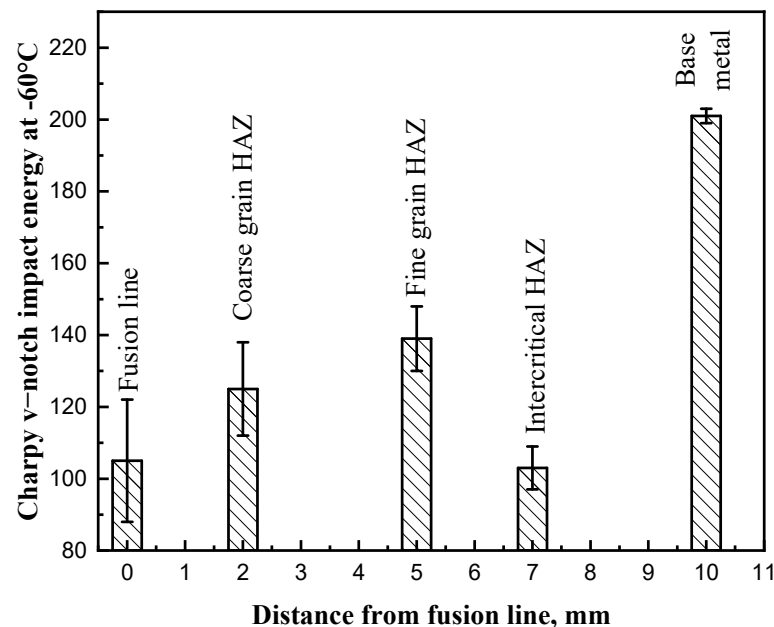

Figure 4. Charpy impact energies at −60 °C of different areas in the studied welded joint.

Figure 5 presents the hardness distribution of the HAZ from the weld metal to base metal with the hardness indentations shown in Figure 2a. The white arrows in Figure 2a indicate representative indentations. It can be seen that the weld metal had a high hardness of ~380 HV0.5. Near the weld metal, the hardness of the CGHAZ had a similarly high value of ~385 HV0.5. In increasing the distance to the FL position to more than ~1.8 mm, the hardness of the CGHAZ decreased gradually to ~320 HV0.5, which was almost equal to the hardness of the FGHAZ. Typically, a smaller grain size will result in higher hardness. However, the hardness of the FGHAZ was usually lower than that of the CGHAZ in the welded joint as revealed by a previous study [28]. This may be caused by the increase in hardenability with increasing the grain size at a high reheating temperature [29]. The hardness of the intercritical HAZ was ~300 HV0.5, which was slightly lower than that of the FGHAZ. In the intercritical HAZ, the microstructure had undergone annealing at the temperature of the two-phase region, which produced some soft annealed bainite, leading to a decrease in hardness, as shown in Figure 3d. However, it is worth noting that the hardness in the FGHAZ was almost the same as that of the base metal (~330 HV0.5). This implies that no obvious softening occurred in the FGHAZ.
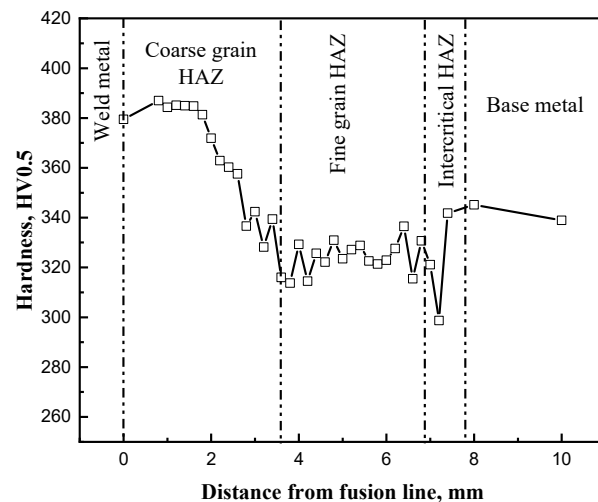
Figure 5. Hardness distribution from weld metal to base metal for studied welded joint.

3.3. EBSD Characterization of Grain Size and Crystallographic Features

In order to elucidate the microstructural origins for the similar high toughness of the CGHAZ and FGHAZ, EBSD analysis was carried out to study the crystallographic features. Through using the EBSD data, the prior austenite grains were reconstructed using the ARPGE software. Figure 6a,b show the inverse pole figures of reconstructed prior austenite grains for the CGHAZ and FGHAZ, respectively. The misorientation of prior austenite grain boundaries was ~15–45°, as shown by the black lines in Figure 6a,b. This is consistent with previous research [30]. It can be visually seen that the largest reconstructed prior austenite grain size was ~150 μm and ~40 μm for CGHAZ and FGHAZ, as indicated by the white star in Figure 6a,b, respectively. According to the reconstructed results, the size distribution of prior austenite grains for the CGHAZ and FGHAZ was plotted by profile, as shown in Figure 6c. It can be found that the prior austenite grain size for the CGHAZ was distributed from ~10 to 150 μm, with a peak at 60–80 μm. The average size of prior austenite grain for the CGHAZ was determined as ~75 μm. For the FGHAZ, the prior austenite grain size was distributed from ~several microns to 50 μm, with a peak at ~15 μm. The average size of prior austenite grain for the FGHAZ was determined as ~15 μm. The average prior austenite grain size for the CGHAZ was five times that of the FGHAZ. This implies that the good low-temperature toughness could be contributed to the fine effective grain size that resulted from the coherent phase transformation [31].

It has been suggested that HAGBs with a misorientation angle (θ) larger than 15° play an important role in refining the effective grain size [32,33]. Hence, the grain boundary distribution with different misorientation angles was studied for the CGHAZ and FGHAZ, and the obtained results are presented in Figure 7. It can be seen that a high density of HAGBs with a misorientation angle greater than 45° was obtained for both the CGHAZ and FGHAZ, as shown by the yellow lines in Figure 7a,b, whereas the boundaries with a misorientation angle between 15 and 45°, which is usually contributed to by prior austenite grain boundaries, was much higher for the FGHAZ than that for the CGHAZ, presented as black lines in Figure 7a,b. The densities of boundaries subjected to different misorientation angles were analyzed as the boundary length per unit area. Statistical analysis results of boundary density for the CGHAZ and FGHAZ are summarized in Figure 7c. The results indicate that there was no significant difference between the CGHAZ and FGHAZ in low-angle grain boundaries (LAGBs, with θ of 5–15°) and high-angle grain boundaries (HAGBs, with θ higher than 45°). The LAGB density was 0.28 and 0.32 $\mu m/\mu m^{-2}$ for the CGHAZ and FGHAZ, respectively. It was 0.79 and 0.76 $\mu m/\mu m^{-2}$ for HAGBs in the CGHAZ and FGHAZ, respectively. The density for medium-angle grain boundaries (MAGBs, with θ of 15–45°) was higher in the FGHAZ (0.35 $\mu m/\mu m^{-2}$) than the CGHAZ (0.16 $\mu m/\mu m^{-2}$). When taking account of the total density of MAGBs and HAGBs, it was

0.95 and 1.11 μm/μm^{-2} for the CGHAZ and FGHAZ, respectively. This implies that a similar fine effective grain size was obtained for both the CGHAZ and FGHAZ in the studied welded joint, resulting in similar low-temperature toughness values.
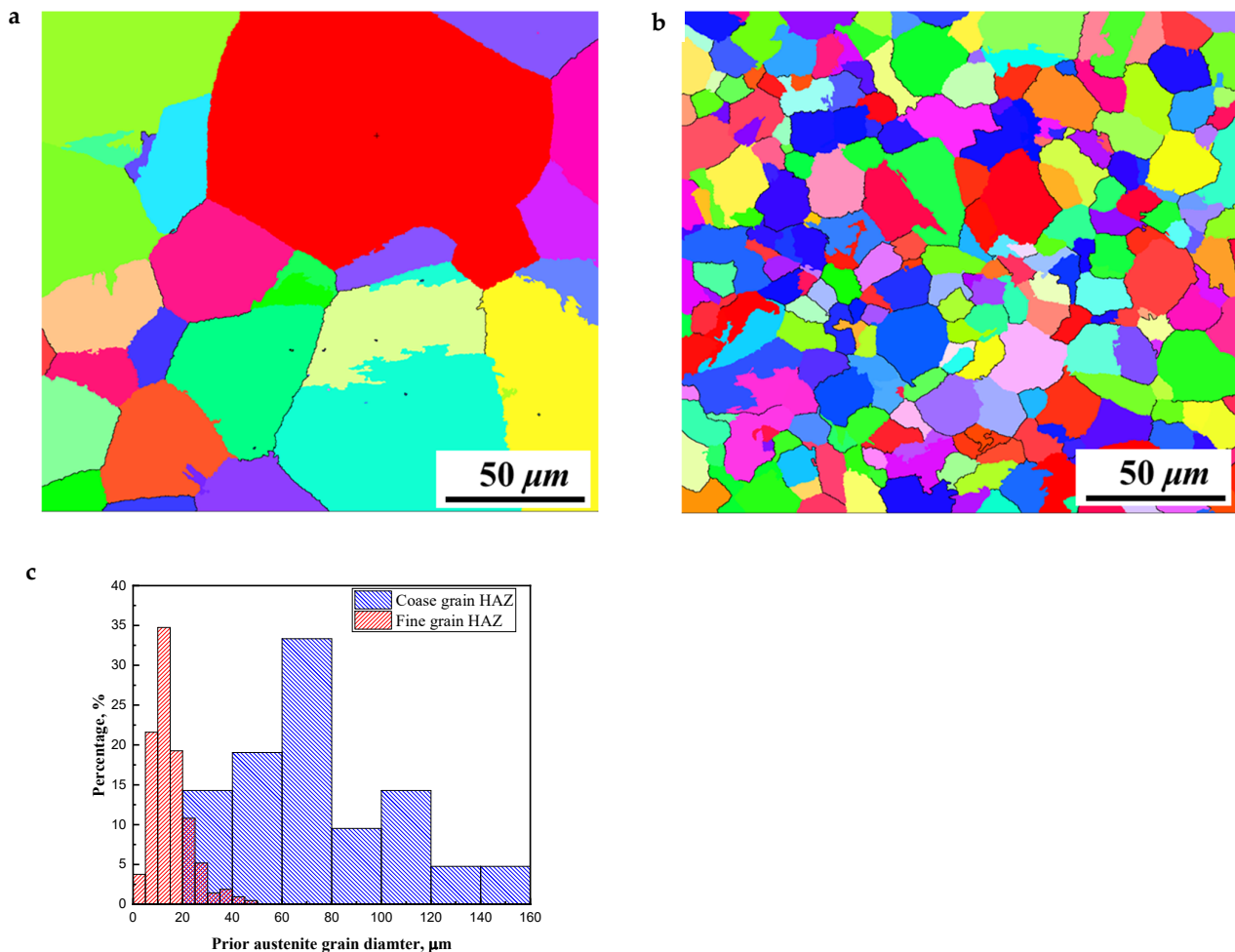

Figure 6. Inverse pole figure of reconstructed austenite grains for CGHAZ (**a**) and FGHAZ (**b**), and (**c**) distribution of reconstructed austenite grain size.

A bainite microstructure is a coherent phase transformation product from austenite. The boundaries for the bainite microstructure could be characterized as the prior austenite grain boundary (PAGB), high-angle (HA, θ ≥ 45°) packet (HA-packet) boundary, low-angle (LA, θ < 45°) packet (LA-packet) boundary, block boundary, and sub-block boundary, according to their crystallographic features. Based on the crystallographic orientation data from EBSD, the diverse crystallographic boundaries for the CGHAZ and FGHAZ were visualized and quantitatively analyzed using a Python program [18]. The obtained results are presented in Figure 8. It can be clearly seen that a high density of grain boundaries was obtained for both the CGHAZ and FGHAZ, as shown in Figure 8a,b, respectively. It can be found that block boundaries were the dominant component among all boundaries for both the CGHAZ and FGHAZ, as shown by red lines in Figure 8a,b. The densities of different boundary types are plotted in Figure 8c. It can be seen that the FGHAZ had higher densities of PAGBs, HA packet boundaries, and LA packet boundaries than the CGHAZ. For block boundaries, the density was higher in the CGHAZ (~0.62 μm/μm^{-2}) than in the FGHAZ (~0.4 μm/μm^{-2}). For sub-block boundaries, the CGHAZ and FGHAZ had a similar density of ~0.2 μm/μm^{-2}. In addition, when taking account of the total density of PAGBs, HA packet boundaries, LA packet boundaries, and block boundaries, it was noted that the CGHAZ and FGHAZ had similar high densities of 0.99 and 0.97 μm/μm^{-2},

respectively. Hence, a similar high impact toughness was obtained for both the CGHAZ and FGHAZ.
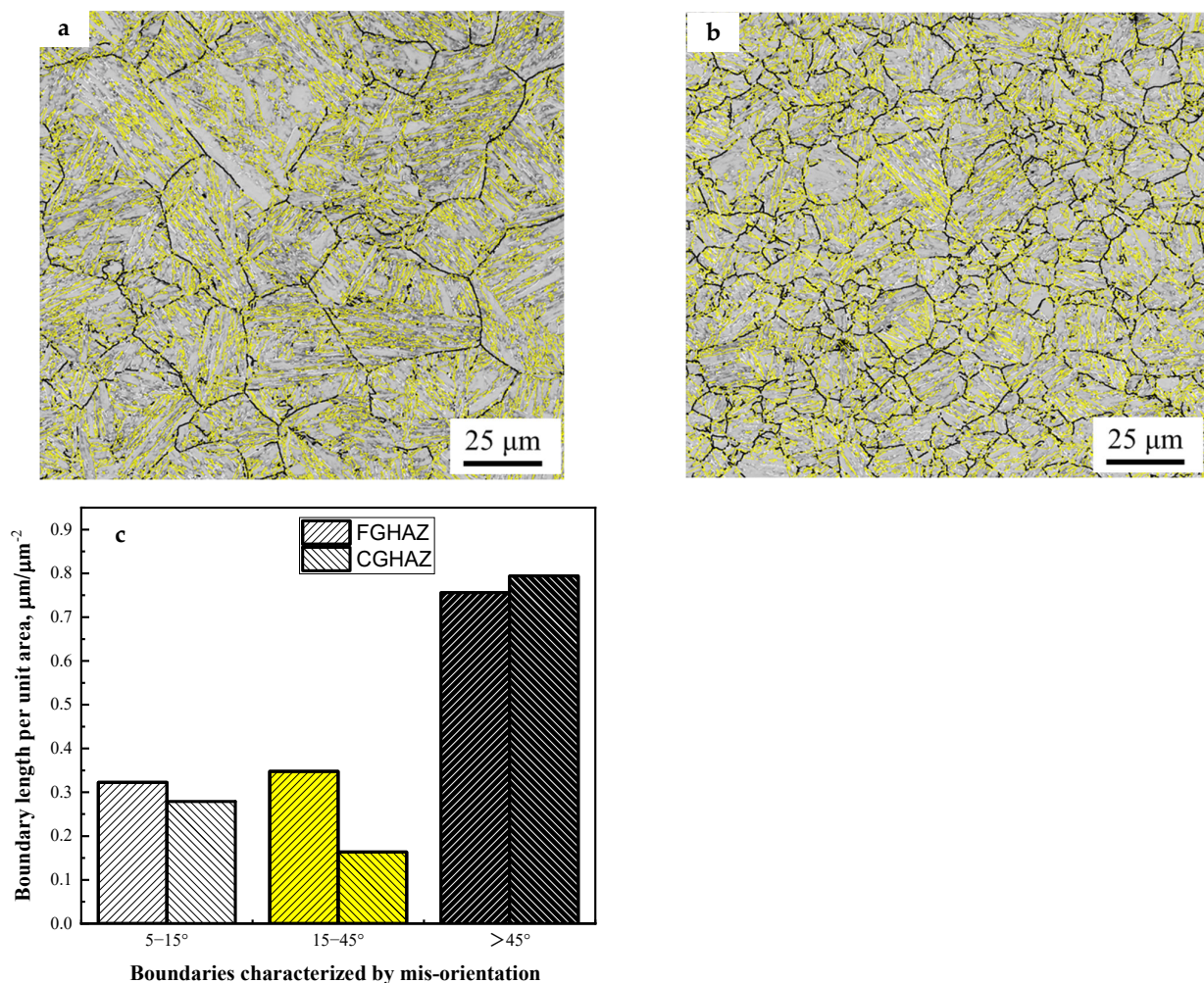

Figure 7. Band contrast (BC) maps depicting distribution of boundaries with different misorientation angles (θ) in (**a**) CGHAZ and (**b**) FCGHAZ, respectively, in which white line: $15° > θ \geq 5°$, black line: $45° > θ > 15°$, yellow line: $θ \geq 45°$; (**c**) densities of boundaries with different misorientation angles.

It is generally known that austenite transforms to bainite via the Kurdjumov–Sachs (K-S) orientation SECrelationship, producing 24 bainitic variants from the perspective of crystallography. According to their pair with variant 1 (V1), different boundary types are defined, as showed in Figure 9 [34–36]. It can be seen that block boundaries are contributed to by variant pairs of V1/V2, V1/V3, V1/V5, and V1/V6, with a misorientation angle of 49.5–60°. A V1/V4 pair consists of sub-block boundaries with a misorientation angle of 10.5°. Other variant pairs with V1 contribute to the formation of packet boundaries, and it can be seen that most of the packet boundaries have a misorientation angle larger than 15°, excluding those from V1/V8, V1/11, and V1/V13 pairs. In the present work, a high density of packet boundaries and block boundaries was obtained for both the CGHAZ and FGHAZ; this indicates that weak variant selection of V1/V4 pairing, which produces low-angle grain boundaries, was obtained for both the CGHAZ and FGHAZ. This is different from the published work on high-strength low-carbon steel without nickel addition, in which a larger grain size induces stronger variant selection of V1/V4 pairing. This may be caused by the difference in the thermo-dynamics of phase transformation due to different nickel alloying designs, and will be discussed later.
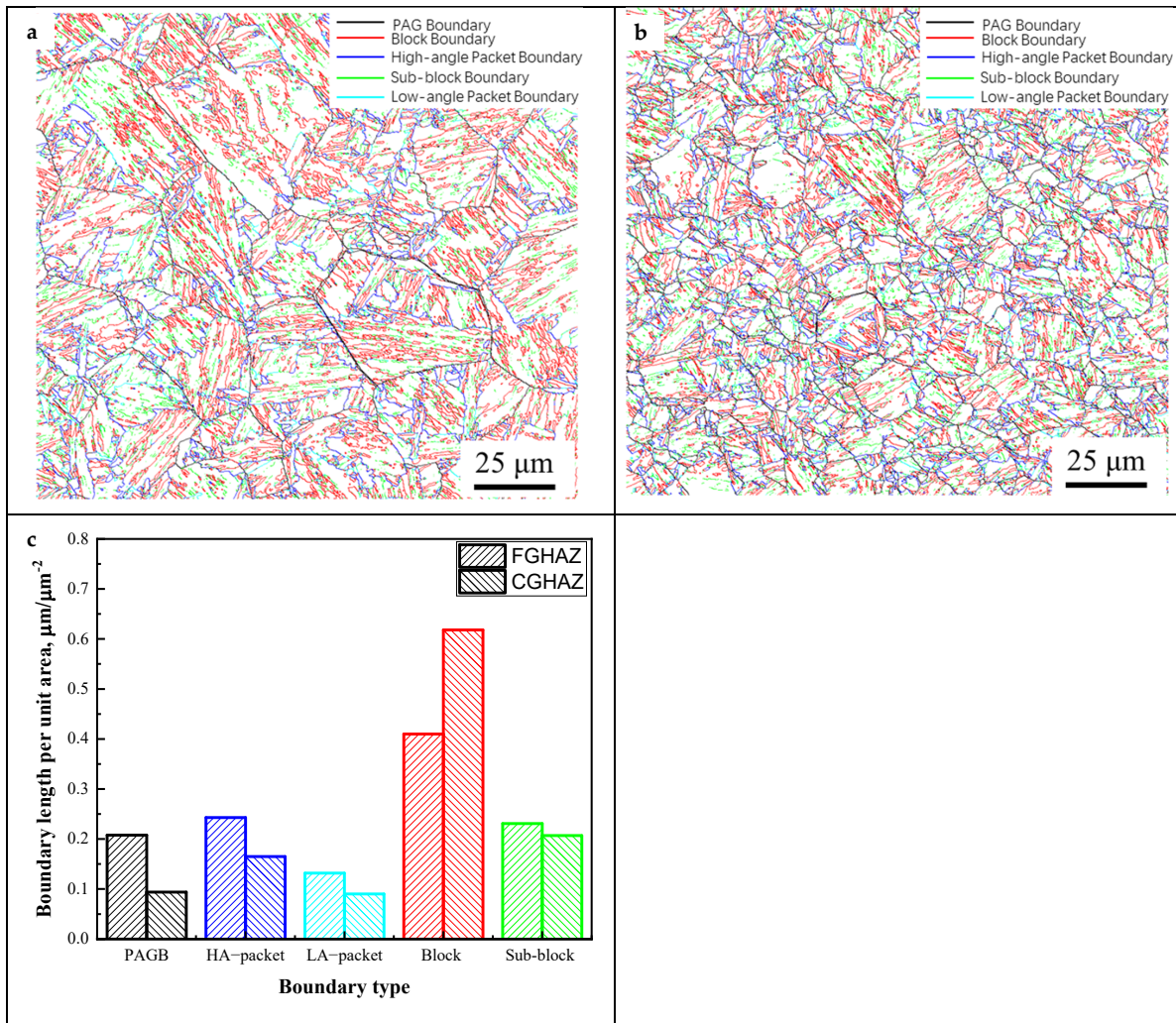
Figure 8. Distribution of different grain boundaries in (**a**) CGHAZ and (**b**) FGHAZ; (**c**) grain boundary density.
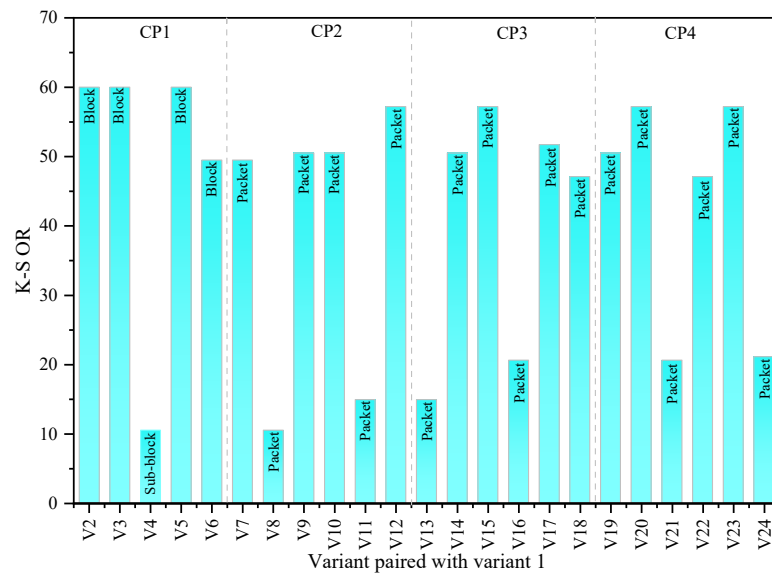

Figure 9. Misorientation angles between V1 and other variants and the intervariant boundary characteristics.

3.4. Thermo-Dynamics for Weak Variant Selection: Benefit of High Nickel Addition

For bainitic phase transformation, variant selection behavior should be controlled by the transformation driving force. It is well known that the cooling rate plays an important role in governing the transformation driving force. A low cooling rate produces a low driving force, and a high cooling rate offers a high driving force. For welding, it has been revealed that a large heat input induces a slow cooling rate, leading to phase transformation at a high temperature with a small driving force, resulting in the strong variant selection of the V1/V4 pair [37]. Another dominant factor governing the transformation driving force is the alloying design. As we mentioned above, a high nickel concentration of 2.5% was alloyed in the steel plate of the studied welded joint. The effect of nickel content on the phase driving force was studied using Thermo-calc (version 2023a) software with the TC-FE9 database. The calculated results are plotted in Figure 10. It can be seen that a high nickel addition induced a low driving force at a given temperature. This implies that phase transformation was difficult at a high temperature for high-nickel alloyed steel, leading to a decrease in bainitic phase transformation. This ensured that the bainitic transformation occurred with a high transformation driving force, leading to weak variant selection of the V1/V4 pair and producing a high density of HAGBs. Therefore, the high nickel addition in the present work was not only helpful for high hardenability but also good for weldability via weaking the variant selection of the V1/V4 pair in the CGHAZ, producing a high toughness for the CGHAZ, as well as the FGHAZ.
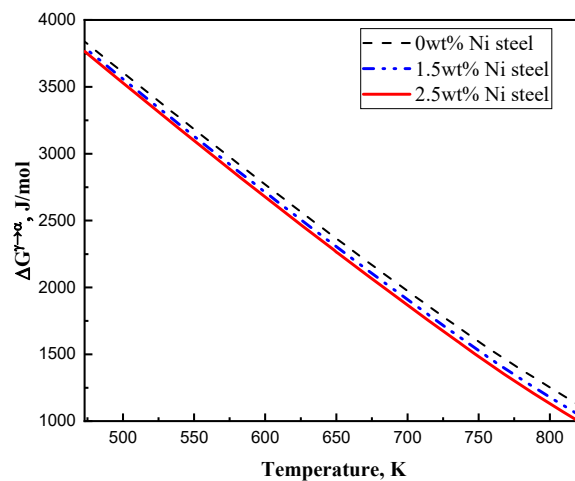

Figure 10. Calculated driving force of austenite (γ) to ferrite (α) for different nickel alloyed steels via Thermo-calc software.

4. Conclusions

In this work, systematical studies were carried out to elucidate the microstructure–property relationship in the HAZ of a FH690 ultra-heavy marine steel plate, with particular emphasis on the insight of the crystallographic features of the CGHAZ and FGHAZ. The obtained main conclusions are summarized as follows:

1. After multi-pass welding with a heat input of ~30 kJ/cm, an ~8 mm wide HAZ was obtained with a CGHAZ of ~3.8 mm, FGHAZ of ~3.4 mm, and intercritical HAZ (ICHAZ) of ~1 mm. The average prior austenite grain size in the CGHAZ and FGHAZ was ~75 and ~15 μm. A fine lath bainite microstructure was obtained for both the CGHAZ and FGHAZ. For the intercritical HAZ, a multiphase microstructure consisting of tempered bainite and fresh bainite was observed.

2. The crystallography analysis revealed that weak variant selection of V1/V4 pairs was obtained for both the CGHAZ and FGHAZ, resulting in a high density of packet boundaries and block boundaries, presenting misorientation angles higher than 15°. Thermo-dynamics calculations indicated that the weak variant selection of V1/V4

pairs was attributed to the decreased phase transformation driving force via high nickel addition.

3. Charpy impact testing results indicate that the fine bainite microstructure with a high density of HAGBs contributed to a good low-temperature toughness for both the CGHAZ and FGHAZ of the studied welded joint. The Charpy impact energies at −60 °C were ~120 and 140 J for the CGHAZ and FGHAZ, respectively. In addition, due to the fine bainitic microstructure in the FGHAZ, a high hardness of ~320 HV0.5 was obtained, which was similar to that of the base metal.

References

1. Mun, D.J.; Shin, E.J.; Choi, Y.W.; Lee, J.S.; Koo, Y.M. Effects of cooling rate, austenitizing temperature and austenite deformation on the transformation behavior of high-strength boron steel. *Mater. Sci. Eng. A* **2012**, *545*, 214–224. [CrossRef]
2. Zhou, T.; Yu, H.; Wang, S.Y. Microstructural Characterization and Mechanical Properties across Thickness of Ultra-Heavy Steel Plate. *Steel Res. Int.* **2017**, *88*, 1700132. [CrossRef]
3. Bian, S.Y.; Zhang, X.; Li, S.L.; Zhang, L.; Li, W.J.; Yan, L. Numerical Simulation, Microstructure, properties of EH40 ultra-heavy plate under gradient temperature rolling. *Mater. Sci. Eng. A* **2020**, *791*, 139778.
4. Revilla, C.; López, B.; Rodriguez-ibabe, J.M. Carbide size refinement by controlling the heating rate during induction tempering in a low alloy steel. *Mater. Des.* **2014**, *62*, 296–304. [CrossRef]
5. Han, P.; Liu, Z.P.; Xie, Z.J.; Wang, H.; Jin, Y.H.; Wang, X.L.; Shang, C.J. Influence of band microstructure on carbide precipitation behavior and toughness of 1 GPa-grade ultra-heavy gauge low-alloy steel. *Int. J. Miner. Metall. Mater.* **2023**, *30*, 1329–1337. [CrossRef]
6. Chen, Y.H.; Sun, S.W.; Zhang, T.M.; Zhou, X.W.; Li, S.H. Effects of post-weld heat treatment on the microstructure and mechanical properties of laser-welded NiTi/304SS joint with Ni filler. *Mater. Sci. Eng. A* **2020**, *771*, 138545. [CrossRef]
7. Chen, Y.H.; Mao, Y.Q.; Lu, W.W.; He, P. Investigation of welding crack in micro laser welded NiTiNb shape memory alloy and Ti6Al4V alloy dissimilar metals joints. *Opt. Laser Technol.* **2017**, *91*, 197–202. [CrossRef]
8. Lee, S.; Kim, B.C.; Lee, D.Y. Fracture mechanism in coarse grained HAZ of HSLA steel welds. *Scr. Metall.* **1989**, *23*, 995. [CrossRef]
9. Davis, C.L.; King, J.E. Cleavage initiation in the intercritically reheated coarse-grained heat-affected zone: Part I. Fractographic evidence. *Metall. Mater. Trans. A* **1994**, *25*, 563–573. [CrossRef]
10. Hu, B.; Wang, Q.M.; Wang, Q.F. Effect of Heat Input on Microstructure and Tensile Properties in Simulated CGHAZ of a V-Ti-N Microalloyed Weathering Steel. *Metals* **2023**, *13*, 1607. [CrossRef]
11. Spachinger, S.J.; Ernst, W.; Enzinger, N. Influence of Ti on the toughness of the FGHAZ and the CGHAZ of high-strength microalloyed S700MC steels. *Weld World* **2017**, *61*, 1117–1131. [CrossRef]
12. Shi, M.H.; Zhang, P.Y.; Zhu, F.X. Toughness and Microstructure of Coarse Grain Heat Affected Zone with High Heat Input Welding in Zr-bearing Low Carbon Steel. *ISIJ Int.* **2014**, *54*, 188–192. [CrossRef]
13. Wang, X.L.; Xie, Z.J.; Su, W.J.; Shang, C.J. Role of Carbon Content on Microstructure Evolution and Impact Toughness in Coarse-Grained Heat-Affected Zone of High-Strength Steel. *Metals* **2023**, *13*, 106. [CrossRef]
14. Wu, B.B.; Wang, Z.Q.; Wang, X.L.; Xu, W.S.; Shang, C.J.; Misra, R.D.K. Toughening of martensite matrix in high strength low alloy steel: Regulation of variant pairs. *Mater. Sci. Eng. A* **2019**, *759*, 430–436. [CrossRef]

15. Sun, S.J.; Du, Y.L.; Zhang, Z.Q.; Jiang, D.Q.; Xu, S.Z.; Ren, Z.M. The Influence of Insertion Depth of Inorganic Materials on Solidification Microstructure and Segregation of 2.5-ton 42CrMo Ingot. *Metals* **2024**, *14*, 753. [CrossRef]

16. Ayçiçek, İ.; Solak, N. Optimization of Macro Segregation and Equiaxed Zone in High-Carbon Steel Use in Prestressed Concrete Wire and Cord Wire Application. *Metals* **2023**, *13*, 1435. [CrossRef]

17. Cayron, C. ARPGE: A computer program to automatically reconstruct the parent grains from electron backscatter diffraction data. *J. Appl. Crystallogr.* **2007**, *40*, 1183–1188. [CrossRef]

18. Li, X.C.; Zhao, J.X.; Cong, J.H.; Misra, R.D.K.; Wang, X.M.; Wang, X.L.; Shang, C.J. Machine learning guided automatic recognition of crystal boundaries in bainitic/martensitic alloy and relationship between boundary types and ductile-to-brittle transition behavior. *J. Mater. Sci. Technol.* **2021**, *84*, 49–58. [CrossRef]

19. Bhadeshia, H.K.D.H.; Keehan, E.; Karlsson, L.; Andrén, H.O. Coalesced bainite. *Trans. Indian I Metals* **2006**, *59*, 689–694.

20. Du, Y.F.; Lu, H.H.; Shen, X.Q. Coupled effects of banded structure and carbide precipitation on mechanical performance of Cr–Ni–Mo–V steel. *Mater. Sci. Eng. A* **2022**, *832*, 142478. [CrossRef]

21. Gáspár, M. Effect of Welding Heat Input on Simulated HAZ Areas in S960QL High Strength Steel. *Metals* **2019**, *9*, 1226. [CrossRef]

22. Tougas, B.; Blais, C.; Chagnon, F.; Pelletier, S. Characterization of Nickel Diffusion and its Effect on the Microstructure of Nickel PM Steels. *Metall. Mater. Trans. A* **2003**, *44*, 754–765. [CrossRef]

23. Luo, H.W.; Qiu, C.H.; Dong, H.; Shi, J. Experimental and numerical analysis of influence of carbide on austenitisation kinetics in 5Mn TRIP steel. *Mater. Sci. Technol.* **2014**, *30*, 1367–1377. [CrossRef]

24. Ma, Y.; Su, L.H.; Shen, C.; Fletcher, L.; Li, H.J.; Sun, L.L.; Zheng, L.; Zhang, C.G. Improving the Weld Heat-Affected-Zone (HAZ) Toughness of High-Strength Thick-Walled Line Pipes. *Metals* **2023**, *13*, 2018. [CrossRef]

25. Huda, N.; Midawi, A.R.H.; Gianetto, J.; Lazor, R. Influence of martensite-austenite (MA) on impact toughness of X80 line pipe steels. *Mater. Sci. Eng. A* **2016**, *662*, 481–491. [CrossRef]

26. Zhu, Z.X.; Han, J.; Li, H.J.; Lu, C. High temperature processed high Nb X80 steel with excellent heat-affected zone toughness. *Mater. Lett.* **2016**, *163*, 171–174. [CrossRef]

27. Wang, J.; Shen, Y.F.; Xue, W.Y.; Jia, N.; Misra, R.D.K. The significant impact of introducing nanosize precipitates and decreased effective grain size on retention of high toughness of simulated heat affected zone (HAZ). *Mater. Sci. Eng. A* **2021**, *803*, 140484. [CrossRef]

28. Poorhaydari, K.; Patchett, B.M.; Ivey, D.G. Microstructure/property examination of weld HAZ in grade 100 microalloyed steel. In Proceedings of the IPC'02: 4th International Pipeline Conference, Calgary, AB, Canada, 29 September–3 October 2002.

29. Han, X.L.; Wu, D.Y.; Min, X.L.; Wang, X.; Liao, B.; Xiao, F.R. Influence of Post-Weld Heat Treatment on the Microstructure, Microhardness, and Toughness of a Weld Metal for Hot Bend. *Metals* **2016**, *6*, 75. [CrossRef]

30. Abbasi, M.; Kim, D.I.; Nelson, T.W.; Abbasi, M. EBSD and reconstruction of pre-transformation microstructures, examples and complexities in steels. *Mater. Charact.* **2014**, *95*, 219–231. [CrossRef]

31. Morris, J.W., Jr.; Guo, Z.; Krenn, C.R.; Kim, Y.H. The Limits of Strength and Toughness in Steel. *ISIJ Int.* **2001**, *41*, 599–611. [CrossRef]

32. Winning, M.; Rollett, A.D. Transition between low and high angle grain boundaries. *Acta Mater.* **2005**, *53*, 2901–2907. [CrossRef]

33. Brandon, D.G. The structure of high-angle grain boundaries. *Acta Metall.* **1996**, *14*, 1479–1484. [CrossRef]

34. Du, J.; Zhang, W.Z.; Dai, F.Z.; Shi, Z.Z. Caution regarding ambiguities in similar ex pressions of orientation relationships. *J. Appl. Crystall.* **2016**, *49*, 40–46. [CrossRef]

35. Takayama, N.; Miyamoto, G.; Furuhara, T. Effects of transformation temperature on variant pairing of bainitic ferrite in low carbon steel. *Acta Mater.* **2012**, *60*, 2387–2396. [CrossRef]

36. Morito, S.; Tanaka, H.; Konishi, R. The morphology and crystallography of lath martensite in Fe-C alloys. *Acta Mater.* **2003**, *51*, 1789–1799. [CrossRef]

37. Stormvinter, A.; Miyamoto, G.; Furuhara, T.; Hedström, P.; Borgenstam, A. Effect of carbon content on variant pairing of martensite in Fe–C alloys. *Acta Mater.* **2012**, *60*, 7265–7274. [CrossRef]